Gigahertz Frequency Antiferromagnetic Resonance and Strong Magnon-Magnon Coupling in the Layered Crystal $CrCl_3$

David MacNeill,[1,*] Justin T. Hou,[2,*] Dahlia R. Klein,[1] Pengxiang Zhang,[2] Pablo Jarillo-Herrero,[1] and Luqiao Liu[2]
[1]*Department of Physics, Massachusetts Institute of Technology, Cambridge, Massachusetts 02139, USA*
[2]*Department of Electrical Engineering and Computer Science, Massachusetts Institute of Technology, Cambridge, Massachusetts 02139, USA*

(Received 5 February 2019; published 24 July 2019)

We report broadband microwave absorption spectroscopy of the layered antiferromagnet $CrCl_3$. We observe a rich structure of resonances arising from quasi-two-dimensional antiferromagnetic dynamics. Because of the weak interlayer magnetic coupling in this material, we are able to observe both optical and acoustic branches of antiferromagnetic resonance in the GHz frequency range and a symmetry-protected crossing between them. By breaking rotational symmetry, we further show that strong magnon-magnon coupling with large tunable gaps can be induced between the two resonant modes.

DOI: 10.1103/PhysRevLett.123.047204

Antiferromagnetic spintronics is an emerging field with the potential to realize high speed logic and memory devices [1–6]. Compared to ferromagnetic materials, antiferromagnetic dynamics are less well understood [7–10], partly due to their high intrinsic frequencies that require terahertz techniques to probe [11–13]. Therefore, antiferromagnetic materials with lower resonant frequencies are desired to enable a wide range of fundamental and applied research [5]. Here, we introduce the layered antiferromagnetic insulator $CrCl_3$ as a tunable platform for studying antiferromagnetic dynamics. Because of the weak interlayer coupling, the antiferromagnetic resonance (AFMR) frequencies are within the range of typical microwave electronics (<20 GHz). This allows us to excite different modes of AFMR and to induce a symmetry-protected mode crossing with an external magnetic field. We further show that a tunable coupling between the optical and acoustic magnon modes can be realized by breaking rotational symmetry. Recently, strong magnon-magnon coupling between two adjacent magnetic layers has been achieved [14,15], with potential applications in hybrid quantum systems [16–18]. Our results demonstrate strong magnon-magnon coupling within a single material and therefore provide a versatile system for microwave control of antiferromagnetic dynamics. Furthermore, $CrCl_3$ crystals can be exfoliated down to the monolayer limit [19] allowing device integration for antiferromagnetic spintronics.

The crystal and magnetic structures of $CrCl_3$ are shown in Fig. 1 [19–26]. Spins within each layer have a ferromagnetic nearest-neighbor coupling of about 0.5 meV, whereas spins in adjacent layers have a weak antiferromagnetic coupling of about 1.6 μeV [25]. Therefore, we can consider each layer as a two-dimensional ferromagnet coupled to the adjacent layers by an interlayer exchange field of roughly 0.1 T [25]. The weak interlayer coupling implies that the field and

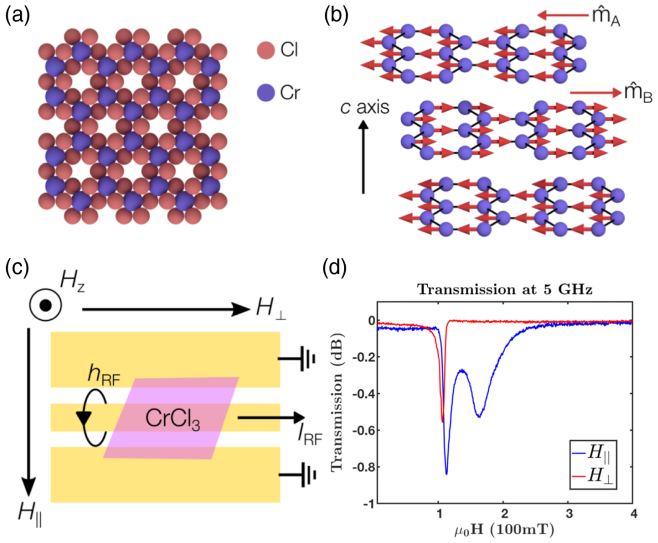

FIG. 1. (a) Crystal structure of a single $CrCl_3$ layer. Red and purple spheres represent chlorine and chromium atoms respectively. (b) Magnetic structure of bulk $CrCl_3$ below the Neél temperature, and without an applied magnetic field. Blue spheres represent the Cr atoms. Red arrows represent the magnetic moment of each Cr atom with parallel intralayer alignment and antiparallel interlayer alignment. The net magnetization direction alternates between layers, having direction $\hat{m}_A$ ($\hat{m}_B$) on layers in the A (B) magnetic sublattice. (c) Experimental schematic featuring a coplanar waveguide (CPW) with a $CrCl_3$ crystal placed over the signal line. $H_{||}$, $H_\perp$, and H_z are the components of the applied dc magnetic field. The microwave transmission coefficient was measured as a function of applied magnetic field and temperature. (d) Typical microwave transmission at 5 GHz and 1.56 K as a function of magnetic field applied parallel (blue) or perpendicular (red) to the in-plane rf field, showing resonances due to AFMR. The two traces were taken from different $CrCl_3$ crystals.

 © 2019 American Physical Society

frequency required to manipulate the antiferromagnetic order parameter (Néel vector) are orders of magnitude lower than in typical antiferromagnets [27–29].

Magnetic resonance measurements of $CrCl_3$ have a long history, including one of the earliest observations of paramagnetic resonance in a crystal [30]. However, the dynamics below the Néel temperature remain largely unexplored. To study this, we first synthesized bulk $CrCl_3$ crystals according to the method of McGuire *et al.* [19,31]. The crystals are transferred to a coplanar waveguide (CPW) and secured with Kapton tape [Fig. 1(c)]. The crystal c axis is normal to the CPW plane. The CPW is mounted in a cryostat and connected to a vector network analyzer by rf cables for microwave transmission measurements. A dc magnetic field is applied with the field directions illustrated in Fig. 1(c). To study the response in the linear regime and to prevent heating, we use a low power excitation signal (estimated to be −35 dBm at the sample).

We measure magnetic resonance by fixing the excitation frequency and sweeping the applied magnetic field. We observe different resonant features in different field geometries [Fig. 1(d)]. Only one resonance is observed when the dc magnetic field is applied perpendicular to the rf field ($H_\perp$), but two resonances show up when the dc magnetic field is applied parallel to the rf field ($H_{||}$). We plot the transmission as a function of excitation frequency and applied magnetic field (Fig. 2). Under $H_{||}$, two modes exist with distinct field dependencies [Fig. 2(a)]: one starting from finite frequency and softening with applied field, and the other with frequency proportional to the applied field. Remarkably, the modes cross without apparent interaction leading to a degeneracy at their crossing point; as we discuss below this crossing is protected by symmetry when the applied field lies in the crystal planes. With $H_\perp$, we see only the linearly dispersing mode [Fig. 2(b)].

To understand the origin of the two modes, we model the magnetic dynamics of $CrCl_3$ in the macrospin approximation. We assume that the magnetization direction is uniform within each layer, and introduce unit vectors $\hat{m}_A$ and $\hat{m}_B$ to represent the magnetization direction on the A and B sublattices. The interlayer exchange energy is approximated as $\mu_0 M_s H_E \hat{m}_A \cdot \hat{m}_B$, where H_E is the interlayer exchange field and M_s is the saturation magnetization. Omitting damping, we get a coupled Landau-Lifshitz-Gilbert (LLG) equation [33]:

$$\frac{d\hat{m}_A}{dt} = -\mu_0\gamma\hat{m}_A \times (\mathbf{H} - H_E\hat{m}_B - M_s(\hat{m}_A \cdot \hat{z})\hat{z}) + \boldsymbol{\tau}_A,$$
$$\frac{d\hat{m}_B}{dt} = -\mu_0\gamma\hat{m}_B \times (\mathbf{H} - H_E\hat{m}_A - M_s(\hat{m}_B \cdot \hat{z})\hat{z}) + \boldsymbol{\tau}_B. \quad (1)$$

Here γ is the gyromagnetic ratio and $\hat{z}$ is the direction perpendicular to sample plane (along the crystal c axis). $\boldsymbol{\tau}_A$ and $\boldsymbol{\tau}_B$ are the torques which arise from the rf field of the CPW.

The term proportional to M_s represents an easy-plane anisotropy arising from the demagnetization field of a platelet shaped crystal. Previous studies have shown that the magnetic anisotropy of $CrCl_3$ is well described by this shape anisotropy [19,25]. Replacing M_s by an effective value would allow for an additional uniaxial magnetocrystalline anisotropy, but we confirm below that this effect is small. We also neglect in-plane anisotropy as the energy depends weakly on the in-plane orientation of the magnetic moments [19,25].

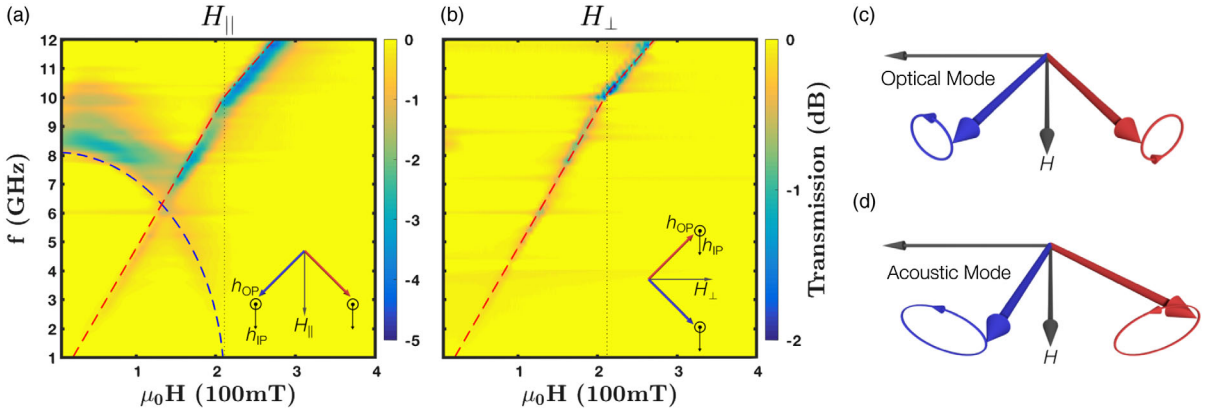

FIG. 2. Microwave transmission as a function of frequency and in-plane magnetic field at 1.56 K with the magnetic field applied (a) parallel and (b) perpendicular to the in-plane rf field (the data for the two panels were taken from different samples). The regions of lower transmission arise from magnetic resonance. Two modes are observed in the $H_{||}$ configuration: an optical mode that has finite frequency at zero applied field, and an acoustic mode with frequency proportional to the applied field. Only the acoustic mode is observed in the $H_\perp$ configuration. Blue and red dashed lines in both panels are fits of the optical and acoustic mode frequencies to Eqs. (2) and (3), respectively. Insets of (a) and (b) show the relative orientation of the dc magnetic field, the equilibrium sublattice magnetizations, and the in-plane (h_{IP}) and out-of-plane (h_{OP}) components of the rf field. (c),(d) Schematic illustrations of the precession orbits for the two sublattice magnetizations in the optical mode and the acoustic mode.

When the magnetic field **H** is applied in the layer plane, Eq. (1) is symmetric under twofold rotation around the applied field direction combined with sublattice exchange [31]. In the linear approximation, this results in two independent modes with even and odd parity under the symmetry (optical mode and acoustic mode; see Fig. 2). The optical and acoustic modes result in Lorentzian resonances centered around the frequencies $\omega_{\pm}$. The frequencies have magnetic field dependence [31,34,35]:

$$\omega_{+} = \mu_0\gamma\sqrt{2H_E M_s\left(1-\frac{H^2}{4H_E^2}\right)}, \tag{2}$$

and

$$\omega_{-} = \mu_0\gamma\sqrt{2H_E(2H_E+M_s)}\,\frac{H}{2H_E}. \tag{3}$$

We can fit the resonance frequencies using Eqs. (2) and (3). These fits are shown by the dashed lines in Fig. 2(a) with fit parameters of $\mu_0 H_E = 105$ mT and $\mu_0 M_s = 396$ mT at $T = 1.56$ K, assuming $\gamma/2\pi \approx 28$ GHz/T for $CrCl_3$ [36]. The observed saturation magnetization is close to 3 μ_B per Cr atom, consistent with magnetometry [19,31] and confirming that the out-of-plane crystalline anisotropy is small. Note that the acoustic mode changes its slope at $\mu_0 H \approx 200$ mT. This occurs because the moments of the two sublattices are aligned with the applied field when $H > 2H_E$ [31]. In this case the crystal behaves as a ferromagnet and the acoustic mode transforms into uniform ferromagnetic resonance (FMR) described by the Kittel formula $\omega_{\mathrm{FMR}} = \mu_0\gamma\sqrt{H(H+M_s)}$. Figures 2(a) and 2(b) also show fits of the data for $H > 2H_E$ to the Kittel formula (dash-dotted line). (The data above and below $H = 2H_E$ are fit simultaneously to extract a consistent parameter set.)

The dependence on field geometry in Fig. 2 can now be understood as a consequence of selection rules. We can state the rule as follows: an rf magnetic field will excite the even (odd) parity mode if it is even (odd) under twofold rotation around the applied field direction [31]. The rf magnetic field generated from the CPW [Fig. 1(c)] has both in-plane and out-of-plane components. Directly over the signal line, the rf field points in the sample plane, while in the gap between the signal line and ground, the rf field is perpendicular to the sample plane. Our crystal is large enough to cover both regions and experience both field directions. In the perpendicular geometry ($H_{\perp}$), both the in-plane and out-of-plane rf fields change sign under twofold rotation around the applied field direction [inset of Fig. 2(b)]. Therefore only the odd parity (acoustic) mode will be excited. In the parallel field geometry ($H_{||}$), the in-plane component is invariant under the twofold rotation and excites the even parity (optical) mode, while the out-of-plane component changes sign and excites the odd-parity (acoustic) mode [inset of Fig. 2(a)]. We will focus on measurements in the parallel field geometry because it allows simultaneous excitation of both modes.

We further study the evolution of the AFMR as a function of temperature. As the temperature is increased from 1.56 K [Fig. 2(a)] to 7 K [Fig. 3(a)], the optical mode frequency decreases due to the reduction of H_E and M_s. The optical mode disappears entirely at 14 K, implying that the sample is no longer antiferromagnetic, consistent with magnetometry measurements [19,31]. At higher temperatures, the magnetic resonance frequency depends linearly on the applied field with a slope of 30.4 GHz/T and 28.8 GHz/T at 21 K and 30 K, respectively [Figs. 3(c) and 3(d)]. This is electron paramagnetic resonance arising from Cr^{3+} ions [36]. In this temperature range, the magnetization is proportional to the applied field through $M = \chi(T)H$. Then the resonant frequency is

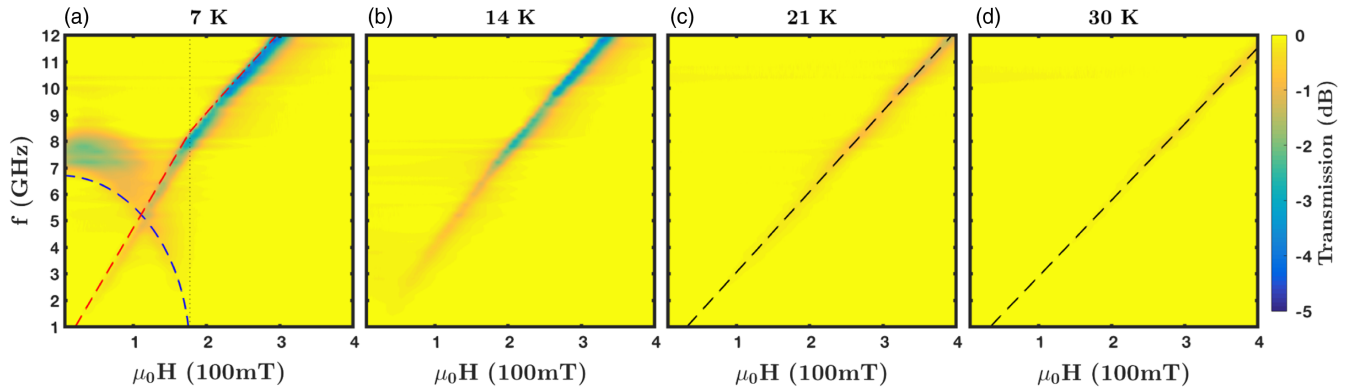

FIG. 3. Microwave transmission as a function of frequency and in-plane magnetic field at 7, 14, 21, and 30 K. At 7 K, the sample is antiferromagnetic and both acoustic and optical modes are observed; $\mu_0 H_E = 89$ mT and $\mu_0 M_s = 323$ mT are determined by fits to Eqs. (2) and (3), which are smaller than those at 1.56 K [Fig. 2(a)]. Only one mode is observed at 14 K, and its frequency does not show a purely linear field dependence. At 21 and 30 K, a single mode with linear field dependence is observed, arising from electron paramagnetic resonance.

$\omega = \mu_0\gamma\sqrt{H(H+M(H,T))} = \mu_0\gamma\sqrt{1+\chi(T)}H$ [37]. Our data correspond to $\chi(21\text{ K}) = 0.178$ and $\chi(30\text{ K}) = 0.056$. For the temperature range 14–20 K, the resonant frequencies do not have a purely linear dependence on applied field [Fig. 3(b)]. This is likely due to a nonlinear relationship $M(H)$ as M approaches its saturation value, previously detected in magnetization and magneto-optical experiments [19,31,38].

So far, we have discussed AFMR with an in-plane applied magnetic field [34]. In this case, the system is symmetric under twofold rotation around the applied field direction combined with sublattice exchange. This prevents hybridization between the optical and acoustic modes, leading to a degeneracy where they cross [see Figs. 2(a) and 3(a)]. In principle, breaking this symmetry can hybridize the two modes and generate an anticrossing gap. One possible approach for inducing symmetry breaking is to use different M_s for the A and B sublattices by stacking different 2D magnets. Here, we instead employ an out-of-plane field to break the 180° rotational symmetry. We measure the AFMR spectrum for a dc magnetic field applied at a range of angles, ψ, from the CPW plane. For $\psi = 30°$, the mode structure is largely unchanged, except that a gap opens near the crossing point [Fig. 4(b)]. Increasing the tilt angle increases the gap size as shown in Fig. 4(c). Therefore, breaking the rotational symmetry with an out-of-plane field introduces a magnon-magnon coupling between the previously uncoupled modes.

To quantitatively describe the magnon-magnon coupling, we turn to the matrix formalism of the LLG equation [31]. The result is high and low frequency branches of antiferromagnetic resonance, continuously connected to the even and odd parity modes. The evolution of both modes and their mixing can be captured by the eigenvalue problem of a two-by-two matrix:

$$\begin{vmatrix} \omega_a^2(H,\psi) - \omega^2 & \Delta^2(H,\psi) \\ \Delta^2(H,\psi) & \omega_o^2(H,\psi) - \omega^2 \end{vmatrix} = 0 \qquad (4)$$

Here $\omega_a = \mu_0\gamma\sqrt{1+(M_s/2H_E)}H\cos\psi$ is the bare acoustic mode frequency and $\omega_o = \mu_0\gamma(2H_EM_s[1-(H^2/H_{\text{FM}}^2)] + \{(\sin^2\psi)/[1+(M_s/2H_E)]^2\}H^2)^{1/2}$ is the bare optical mode frequency. H_{FM} is the applied magnetic field required to fully align the two sublattices, satisfying $1/H_{\text{FM}}^2 = \cos^2\psi/(2H_E)^2 + \sin^2\psi/(2H_E+M_s)^2$. $\Delta = \mu_0\gamma H[2H_E/(2H_E+M_s)\sin^2\psi\cos^2\psi]^{1/4}$ represents the magnon-magnon coupling term. The solutions of Eq. (4) are the resonance frequencies of the LLG equation. When $|\omega_o - \omega_a| \gg \Delta$, the effect of the coupling term is negligible and the solutions are approximately $\omega \approx \omega_o$ and $\omega \approx \omega_a$. When the optical and acoustic modes become closer in frequency, they are hybridized by the coupling term opening a gap. This coupling is zero for $\psi = 0°$ and only becomes nonzero as we cant the applied field out-of-plane. Note that when $\psi = 90°$ the mode coupling is zero again corresponding to rotational symmetry around the out-of-plane direction [31]; this decoupling becomes relevant for $\psi > 80°$ so we will focus on the regime $\psi < 80°$.

The dashed lines in Figs. 4(a)–4(c) indicate fits to the eigenvalues of Eq. (4), with fit parameters $\mu_0M_s = 409$ mT and $\mu_0H_E = 101$ mT. The coupling strength $g/2\pi$ is determined as half of the minimal frequency spacing in the fits. We determine the dissipation rates of the upper and lower branches, κ_U and κ_L, by Lorentzian fitting of the frequency dependence of the transmission, using vertical cuts on the 2D plots of 4(c). For $\psi = 55°$, we obtain $g/2\pi \approx 0.8$ GHz, $\kappa_U/2\pi \approx 0.5$ GHz, and $\kappa_L/2\pi \approx 0.2$ GHz which indicates strong magnon-magnon coupling as $g > \kappa_U$ and $g > \kappa_L$ [14]. The cooperativity is $C = g^2/(\kappa_U \times \kappa_L) = 6.4$, which can be improved by using a more homogeneous sample. Figure 4(e) shows the angular dependence of g. By rotating the crystal alignment in an

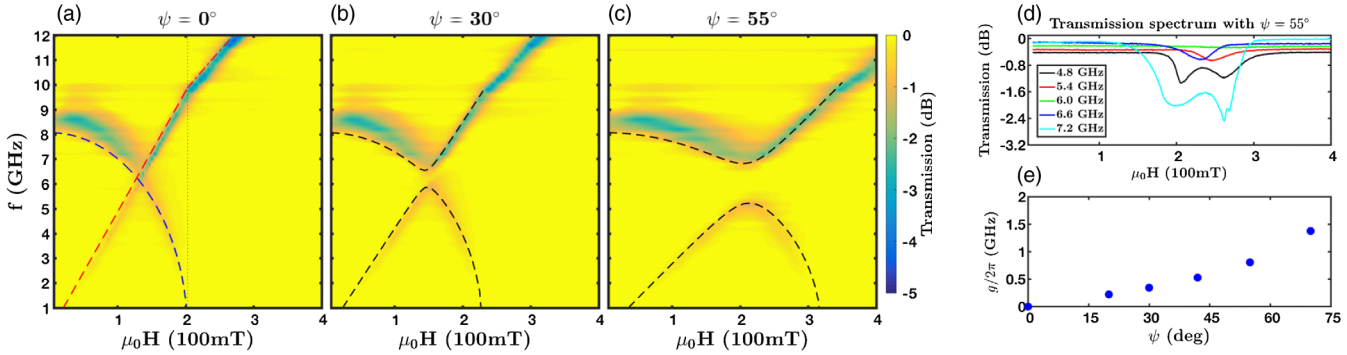

FIG. 4. Microwave transmission as a function of frequency and applied field at 1.56 K; the field is applied at an angle of (a) $\psi = 0°$, (b) 30°, and (c) 55° from the sample plane. When the field is applied in-plane, the mode crossing is protected by rotational symmetry combined with sublattice exchange. Out-of-plane field breaks the symmetry and couples the two modes resulting in tunable gaps. (d) Microwave transmission vs applied field at $\psi = 55°$ for various frequencies, showing the coupling gap. An extra small dip appears at 7.2 GHz, probably due to resonance peak splitting induced by inhomogeneities. (e) The coupling strength g increases with ψ, and can be tuned from 0 to 1.37 GHz.

applied field, we can tune the system from a symmetry-protected mode crossing to the strong coupling regime.

In summary, we have measured magnetic resonance of the layered antiferromagnet $CrCl_3$ as a function of temperature and applied magnetic field, with the magnetic field applied at various angles from the crystal planes. We have shown that $CrCl_3$ possess a rich GHz-frequency AFMR spectrum due to the weak interlayer coupling. We detect both acoustic and optical branches of AFMR and show that an applied magnetic field can induce an accidental degeneracy between them. Furthermore, by breaking rotational symmetry we can induce a coupling between these modes and open a tunable gap. All of these effects are captured with analytical solutions to the LLG equation. We also expect interaction between the modes in the nonlinear regime. For example, three-magnon processes could be triggered when the frequencies of the acoustic and optical modes satisfy certain relationships.

There is also tremendous interest in isolating ultrathin layered magnets using mechanical exfoliation [39,40], and incorporating them in van der Waals heterostructures [41,42]. Because $CrCl_3$ can be cleaved to produce air-stable films down to the monolayer limit [19], we expect our results to enable device-based antiferromagnetic spintronics with microwave control of the Néel vector. Our results apply broadly within the class of transition metal trihalides, so that the frequency scale can be tuned by varying the chemical composition and thickness [19]. Using van der Waals assembly, we can combine different magnetic materials to induce magnon-magnon coupling without out-of-plane field by breaking sublattice exchange symmetry.

Device fabrication, data analysis, and measurements by the PJH group were primarily supported by the DOE Office of Science, Basic Energy Sciences under Award No. DE-SC0018935 (D. M.), as well as the Gordon and Betty Moore Foundations EPiQS Initiative through Grant No. GBMF4541 to P. J.-H. Crystal growth was partly supported by the Center for Integrated Quantum Materials under NSF Grant No. DMR-1231319 (D. R. K.). D. R. K. acknowledges partial support by the NSF Graduate Research Fellowship Program under Grant No. 1122374. J. T. H., P. Z., and L. L. acknowledge support from National Science foundation under Grant No. ECCS-1808826.

[*] These authors contributed equally to this work.

[1] T. Jungwirth, X. Marti, P. Wadley, and J. Wunderlich, Nat. Nanotechnol. **11**, 231 (2016).
[2] P. Wadley *et al.*, Science **351**, 587 (2016).
[3] N. Bhattacharjee, A. A. Sapozhnik, S. Y. Bodnar, V. Y. Grigorev, S. Y. Agustsson, J. Cao, D. Dominko, M. Obergfell, O. Gomonay, J. Sinova, M. Kläui, H.-J. Elmers, M. Jourdan, and J. Demsar, Phys. Rev. Lett. **120**, 237201 (2018).
[4] V. Baltz, A. Manchon, M. Tsoi, T. Moriyama, T. Ono, and Y. Tserkovnyak, Rev. Mod. Phys. **90**, 015005 (2018).
[5] R. A. Duine, K.-J. Lee, S. S. P. Parkin, and M. D. Stiles, Nat. Phys. **14**, 217 (2018).
[6] K. Olejník, T. Seifert, Z. Kašpar, V. Novák, P. Wadley, R. P. Campion, M. Baumgartner, P. Gambardella, P. Němec, J. Wunderlich, J. Sinova, P. Kužel, M. Müller, T. Kampfrath, and T. Jungwirth, Sci. Adv. **4**, eaar3566 (2018).
[7] R. Cheng, J. Xiao, Q. Niu, and A. Brataas, Phys. Rev. Lett. **113**, 057601 (2014).
[8] Q. Liu, H. Y. Yuan, K. Xia, and Z. Yuan, Phys. Rev. Mater. **1**, 061401 (2017).
[9] R. Cheng, D. Xiao, and A. Brataas, Phys. Rev. Lett. **116**, 207603 (2016).
[10] A. Kamra and W. Belzig, Phys. Rev. Lett. **119**, 197201 (2017).
[11] N. Bhattacharjee, A. A. Sapozhnik, S. Y. Bodnar, V. Y. Grigorev, S. Y. Agustsson, J. Cao, D. Dominko, M. Obergfell, O. Gomonay, J. Sinova, M. Kläui, H.-J. Elmers, M. Jourdan, and J. Demsar, Phys. Rev. Lett. **120**, 237201 (2018).
[12] T. Kampfrath, A. Sell, G. Klatt, A. Pashkin, S. Mhrlein, T. Dekorsy, M. Wolf, M. Fiebig, A. Leitenstorfer, and R. Huber, Nat. Photonics **5**, 31 (2011).
[13] S. Baierl, J. H. Mentink, M. Hohenleutner, L. Braun, T.-M. Do, C. Lange, A. Sell, M. Fiebig, G. Woltersdorf, T. Kampfrath, and R. Huber, Phys. Rev. Lett. **117**, 197201 (2016).
[14] J. Chen, C. Liu, T. Liu, Y. Xiao, K. Xia, G. E. W. Bauer, M. Wu, and H. Yu, Phys. Rev. Lett. **120**, 217202 (2018).
[15] S. Klingler, V. Amin, S. Geprags, K. Ganzhorn, H. Maier-Flaig, M. Althammer, H. Huebl, R. Gross, R. D. McMichael, M. D. Stiles, S. T. B. Goennenwein, and M. Weiler, Phys. Rev. Lett. **120**, 127201 (2018).
[16] X. Zhang, C.-L. Zou, L. Jiang, and H. X. Tang, Phys. Rev. Lett. **113**, 156401 (2014).
[17] L. Bai, M. Harder, Y. P. Chen, X. Fan, J. Q. Xiao, and C.-M. Hu, Phys. Rev. Lett. **114**, 227201 (2015).
[18] Y. Tabuchi, S. Ishino, A. Noguchi, T. Ishikawa, R. Yamazaki, K. Usami, and Y. Nakamura, Science **349**, 405 (2015).
[19] M. A. McGuire, G. Clark, S. KC, W. M. Chance, G. E. Jellison, V. R. Cooper, X. Xu, and B. C. Sales, Phys. Rev. Mater. **1**, 014001 (2017).
[20] M. A. McGuire, Crystals **7**, 121 (2017).
[21] J. W. Cable, M. K. Wilkinson, and E. O. Wollan, J. Phys. Chem. Solids **19**, 29 (1961).
[22] A. Narath, Phys. Rev. **131**, 1929 (1963).
[23] H. L. Davis and A. Narath, Phys. Rev. **134**, A433 (1964).
[24] A. Narath, Phys. Rev. **140**, A854 (1965).
[25] A. Narath and H. L. Davis, Phys. Rev. **137**, A163 (1965).
[26] E. J. Samuelsen, R. Silberglitt, G. Shirane, and J. P. Remeika, Phys. Rev. B **3**, 157 (1971).
[27] F. M. Johnson and A. H. Nethercot, Phys. Rev. **114**, 705 (1959).
[28] H. Kondoh, J. Phys. Soc. Jpn. **15**, 1970 (1960).
[29] A. J. Sievers and M. Tinkham, Phys. Rev. **129**, 1566 (1963).
[30] N. F. Ramsey, Phys. Perspect. **1**, 123 (1999).

[31] See Supplemental Material at http://link.aps.org/supplemental/10.1103/PhysRevLett.123.047204 for discussions of the sample preparation, theoretical analysis, and magnetometry data, which includes Refs. [19,32].
[32] C. Kittel, Phys. Rev. **73**, 155 (1948).
[33] F. Keffer and C. Kittel, Phys. Rev. **85**, 329 (1952).
[34] V. S. Mandel, V. D. Voronkov, and D. E. Gromzin, Sov. Phys. JETP **36**, 521 (1973).
[35] P. K. Streit and G. E. Everett, Phys. Rev. B **21**, 169 (1980).
[36] S. Chehab, J. Amiell, P. Biensan, and S. Flandrois, Physica (Amsterdam) **173B**, 211 (1991).
[37] J.-L. Stanger, J.-J. Andrė, P. Turek, Y. Hosokoshi, M. Tamura, M. Kinoshita, P. Rey, J. Cirujeda, and J. Veciana, Phys. Rev. B **55**, 8398 (1997).
[38] B. Kuhlow, Phys. Status Solidi (a) **72**, 161 (1982).
[39] B. Huang, G. Clark, E. Navarro-Moratalla, D. R. Klein, R. Cheng, K. L. Seyler, D. Zhong, E. Schmidgall, M. A. McGuire, D. H. Cobden, W. Yao, D. Xiao, P. Jarillo-Herrero, and X. Xu, Nature (London) **546**, 270 (2017).
[40] C. Gong, L. Li, Z. Li, H. Ji, A. Stern, Y. Xia, T. Cao, W. Bao, C. Wang, Y. Wang, Z. Q. Qiu, R. J. Cava, S. G. Louie, J. Xia, and X. Zhang, Nature (London) **546**, 265 (2017).
[41] D. R. Klein, D. MacNeill, J. L. Lado, D. Soriano, E. Navarro-Moratalla, K. Watanabe, T. Taniguchi, S. Manni, P. Canfield, J. Fernández-Rossier, and P. Jarillo-Herrero, Science **360**, 1218 (2018).
[42] T. Song, X. Cai, M. W.-Y. Tu, X. Zhang, B. Huang, N. P. Wilson, K. L. Seyler, L. Zhu, T. Taniguchi, K. Watanabe, M. A. McGuire, D. H. Cobden, D. Xiao, W. Yao, and X. Xu, Science **360**, 1214 (2018).